Journal of the Korean Society of Surveying, Geodesy, Photogrammetry and Cartography
Vol. 37, No. 5, 323-330, 2019
https://doi.org/10.7848/ksgpc.2019.37.5.323

ISSN 1598-4850(Print)
ISSN 2288-260X(Online)
Original article

Local-Based Iterative Histogram Matching for Relative Radiometric Normalization

Seo, Dae Kyo [1] · Eo, Yang Dam [2]

Abstract

Radiometric normalization with multi-temporal satellite images is essential for time series analysis and change detection. Generally, relative radiometric normalization, which is an image-based method, is performed, and histogram matching is a representative method for normalizing the non-linear properties. However, since it utilizes global statistical information only, local information is not considered at all. Thus, this paper proposes a histogram matching method considering local information. The proposed method divides histograms based on density, mean, and standard deviation of image intensities, and performs histogram matching locally on the sub-histogram. The matched histogram is then further partitioned and this process is performed again, iteratively, controlled with the wasserstein distance. Finally, the proposed method is compared to global histogram matching. The experimental results show that the proposed method is visually and quantitatively superior to the conventional method, which indicates the applicability of the proposed method to the radiometric normalization of multi-temporal images with non-linear properties.

Keywords : Local-Based Iterative Histogram Matching, Wasserstein Distance, Relative Radiometric Normalization, Non-Linear

1. Introduction

With the recent development of various satellite sensors, it is feasible to acquire multi-temporal satellite images with which the Earth's surface can be monitored (Zhong *et al.*, 2016). Change detection is a representative remote sensing technique that quantitatively analyzes the change in the target area using multi-temporal satellite imagery (Choi, 2015). However, these images are strongly affected by several factors, including atmospheric conditions, sun-target-sensor illumination geometry, and sensor characteristics (Chen *et al.*, 2005; Hong and Zhang, 2008). Thus, to detect accurate changes using multi-temporal datasets, it is necessary to use preprocessing methods to reduce the radiometric variances resulting from the aforementioned effects (Song *et al.*, 2001). One of these is radiometric normalization, which is typically divided into absolute and relative methods (Du *et al.*, 2002). Absolute radiometric correction requires sensor calibration parameters and atmospheric properties at the time of data acquisition, which is difficult to obtain due to cost or accessibility (Liu *et al.*, 2007). However, relative radiometric normalization aims to reduce radiometric differences by normalizing the radiometric characteristics of a subject image compared to a reference image. Therefore, relative radiometric normalization that does not require in-situ data is generally utilized (Biday and Bhosle, 2010).

Relative radiometric normalization can be divided into linear-based and non-linear-based methods (Chen *et al.*, 2018). The linear-based methods assume a linear relationship between pixels at the same position, based on

Received 2019. 09. 23, Revised 2019. 10. 07, Accepted 2019. 10. 24
1) Member, Dept. of Advanced Technology Fusion, Konkuk University (E-mail: tjeory@konkuk.ac.kr)
2) Corresponding Author, Member, Dept. of Technology Fusion Engineering, Konkuk University (E-mail: eoandrew@konkuk.ac.kr)

linear regression, and contains MM (Minimum-Maximum), MS (Mean-Standard deviation), DB (Dark-set-Bright set), NC (No-Change set), and PIF (Pseudo Invariant Feature) (Charvez, 1988; Elvidge *et al.*, 1995; Schott *et al.*, 1988; Yang and Lo, 2000; Yuan and Elvidge, 1996). However, most remote sensing data has a non-linear distribution, and the actual Earth's surface consists of natural and artificial features that exhibit complex and non-linear properties (Seo *et al.*, 2017). The spectral differences caused by the growth of vegetation, in particular, have radiometric properties including representative non-linearity (Bai *et al.*, 2018). Thus, for these methods, normalization does not occur properly in the presence of non-linear radiometric properties caused by differences in vegetation (Seo and Eo, 2018). The non-linear-based methods consider the non-linear relationship between multi-temporal images, typically histogram matching (Hermel and Ruefenacht, 2007). This approach is a non-linear matching of the histograms of the subject image such that they have a distribution similar to those of the reference image; this allows the radiometric properties to be normalized in the presence of non-linear properties. However, histogram matching does not take local properties into account since only global statistical information is utilized; therefore, it becomes less flexible for radiometric normalization (Bai *et al.*, 2018).

To overcome these limitations, this study proposes a histogram-matching-based relative radiometric normalization method that considers local information. The proposed method divides the histogram according to density, mean, and standard deviation, and performs histogram matching locally on the sub-histograms. The resulting matched histogram is again divided into several parts to allow the consideration of more local properties. The process is performed iteratively and controlled by the wasserstein distance. Finally, in order to verify the applicability of the proposed method, it is evaluated by comparing it to the results of conventional global histogram matching.

2. Methodology

2.1 Histogram matching

Histogram matching transforms the histogram distribution of the subject image to the specified histogram of the reference image such that the radiometric properties in the two images correspond as closely as possible. It is based on the CDF (Cumulative Distribution Function), in which the pixel values of a reference image are assigned to the pixel values of a subject image upon their conversion into a frequency distribution (Helmer and Ruefenacht, 2007). For example, if *u* and *v* are the subject and the reference images, respectively, composed of gray levels in the range of [0, *L*-1], the CDFs of the subject and reference images are defined as in Eqs. (1) and (2):

$$s_k = C_u(u_k) = \sum_{i=0}^{k} P(u_i) = \sum_{i=0}^{k} \frac{n_i}{n} \tag{1}$$

$$r_k = C_v(v_k) = \sum_{i=0}^{k} P(v_i) \tag{2}$$

where s_k and r_k are the histograms of the subject and reference images, respectively; $C_u(u_k)$ and $C_v(v_k)$ are the CDFs of the subject and reference images, respectively; $P(u_i)$ and $P(v_i)$ are the gray level probabilities of histogram and represents the probability distribution function; n_k is the number of pixels with gray level k; and n is the total number of pixels in the image (Sun *et al.*, 2005). Then the smallest integer number between s_k and r_k is determined using Eq. (3), defined as follows:

$$(C_v(v_k) - s_k) = (r_k - s_k) \rightarrow 0 \tag{3}$$

This represents $r_k = s_k$, and, given the above, results in $v_k = C_v^{-1}(r_k) = C_v^{-1}(C_u(u_k))$. Finally, k is replaced with k', as shown in Eq. (4):

$$k' = C_v^{-1}(C_u(u_k)) \tag{4}$$

2.2 Local-based iterative histogram matching

The proposed method can be decomposed into three main stages: (1) histogram division, (2) local-based histogram matching, and (3) calculation of wasserstein distance. In the first stage, the histogram is divided into several parts to allow local calculation of the transformation function. The thresholds of the division are obtained according to the

density, mean, and standard deviation of the image intensities (Shakeri *et al.*, 2018). If the intensities for the subject and references images are in the $[a_u, b_u]$ and $[a_v, b_v]$ intervals, the first step is to calculate the mean and standard deviation of each image. Then, based on these results, two threshold values to separate the histogram are calculated, respectively, as shown in Eqs. (5) and (6):

$$T_{u1} = \mu_u - \sigma_u,\ T_{u2} = \mu_u + \sigma_u \tag{5}$$

$$T_{v1} = \mu_v - \sigma_v,\ T_{v2} = \mu_v + \sigma_v \tag{6}$$

where T_{u1} and T_{u2} are the lower and upper thresholds of the subject image; T_{v1} and T_{v2} are the lower and upper thresholds of the reference image; μ_u and σ_u are the mean and standard deviation of the subject image; and μ_v and σ_v are the mean and standard deviation of the reference image. In local-based histogram matching, histogram matching is performed locally on the intervals of $[a_u, T_{u1}]$, $[T_{u1}+1, T_{u2}-1]$, and $[T_{u2}, b_u]$ with the corresponding intervals of the $[a_v, T_{v1}]$, $[T_{v1}+1, T_{v2}-1]$, and $[T_{v2}, b_v]$, which leads to acquisition of an initial locally matched histogram. The wasserstein distance, which is the stopping criterion for this algorithm, measures the discrepancy between the two distributions (Rabin *et al.*, 2011). It is more adequate for calculating similarity structures than other metrics and is effective for use with probability distributions (Rostami *et al.*, 2019). It performs exceptionally well at capturing human perception of similarity in particular (Rubner, *et al.*, 2000). Given two distributions u_d and v_d on spatial coordinates R, the wasserstein distance between them is defined as given in Eq. (7):

$$W(u_d, v_d) = \inf_{\gamma \in \Pi(u_d, v_d)} \int_{R \times R} c(x, y)\, d\gamma(x, y) \tag{7}$$

where $\Pi(u_d, v_d)$ is the set of joint distributions whose marginals are u_d and v_d; and $c(x, y)$ is the cost function, which is $|x - y|$ in this paper.

The algorithm is then repeated again, from the first step, for the initial locally matched histogram; the histograms are further partitioned to account for more local properties. If $[a_{u'}, b_{u'}]$ are the intervals of the initial locally matched histogram, it is first divided into $[a_{u'}, T_{u'1^{(1)}}]$, $[T_{u'1^{(1)}}+1, T_{u'2^{(1)}}-1]$, and $[T_{u'2^{(1)}}, b_{u'}]$ in the same manner as the initial histogram division. Then, the interval $[T_{u'1^{(1)}}+1, T_{u'2^{(1)}}-1]$ is subdivided by replacing the value $a_{u'}$ with $T_{u'1^{(1)}}+1$ and $b_{u'}$ with $T_{u'2^{(1)}}-1$. The histogram division is then repeated again, leading to a result of $[a_{u'}, T_{u'1^{(1)}}]$, $[T_{u'1^{(1)}}+1, T_{u'1^{(2)}}]$, $[T_{u'1^{(2)}}+1, T_{u'2^{(2)}}-1]$, $[T_{u'2^{(2)}}, T_{u'2^{(1)}}-1]$, and $[T_{u'2^{(1)}}, b_{u'}]$. Histogram matching is performed locally in a similar manner to obtain the next locally matched histogram, which also calculates the wasserstein distance with the histogram of the reference image. Then, if the distance of the latter is larger, the algorithm is stopped and the former is adopted as the final matched histogram; otherwise, the algorithm from the previous step is repeated for the latter histogram. In other words, the algorithm is repeated until there is no improvement in the wasserstein distance in the ith step of applying algorithm where $i = 1, 2, \ldots, t$, the interval is divided into $[a_{u'}, T_{u'1^{(1)}}]$, $[T_{u'1^{(1)}}+1, T_{u'1^{(2)}}]$, $\cdots [T_{u'1^{(t)}}+1, T_{u'2^{(t)}}-1]$, $\cdots$, $[T_{u'2^{(2)}}, T_{u'2^{(1)}}-1]$, and $[T_{u'2^{(1)}}, b_{u'}]$. The detailed process of the proposed method is summarized in Fig. 1.

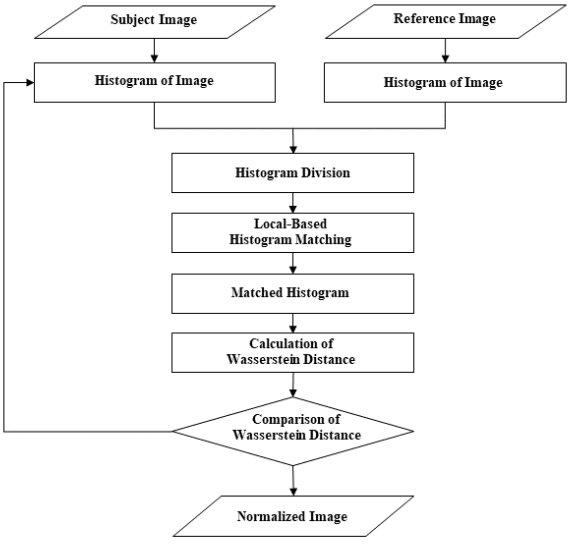

Fig. 1. The details of the proposed method

3. Results and Analysis

3.1 Dataset

The images for the experimental dataset in this study were acquired using the high-resolution sensor on the KOMPSAT (Korea Multi-Purpose Satellite)-3 and 3A. The KOMPSAT-3 and KOMPSAT-3A have the same spectral response functions and main difference is only spatial resolution. Therefore, the experiment is performed by resampling KOMPSAT-3 at 2.2 m, which is the same resolution as KOMPSAT-3A. The product level is L1G; it is processed using radiometric, sensor, and geometric correction techniques and projected to the Universal Transverse Mercator projection system.

Two study sites were selected. Site 1 is located in Changnyeong-gun (southeastern South Korea), which consists of forests, crops, barren lands, water, and built-up areas. The subject and reference images were acquired on October 30, 2015 and June 18, 2016, respectively, from KOMPSAT-3A. Site 2 is located in Seoul, which mainly consists of forests and built-up areas. The subject and reference images for this site were acquired on February 23, 2017 and October 9, 2015 from KOMPSAT-3A and KOMPSAT-3, respectively. In particular, there is a difference in vegetation in each pair to identify the effects of nonlinear properties on the normalization. After the acquisition, image registration was performed by identifying 25 ground control points in each pair and a first-order polynomial combined with the nearest-neighbor resampling was used as a warping method, which satisfied the requirement of less than 0.5 pixels for the RMSE (Root Mean Squared Error). Furthermore, the image sizes for the experiments were set at 2000×2000 and 2000×1500 pixels for Sites 1 and 2, respectively. The details of the dataset are provided in Table 1 and the experimental images for each site are shown in Figs. 2 and 3.

(a) (b)

Fig. 2. The experimental images of Site 1: (a) subject image (2015.10.30.), (b) reference image (2016.06.18.)

(a) (b)

Fig. 3. The experimental images of Site 2: (a) subject image (2017.02.23.), (b) reference image (2015.10.09.)

3.2 Experimental results

This section presents the results of histogram matching with local characteristics and compares it with global histogram matching. The proposed method was applied stepwise on the experimental images for each band. For Site 1, as a result of histogram division, bands 1, 2, 3, and 4 are applied 4, 7, 7,

Table 1. Specification of the dataset

Image pairs	Sensor	Date	Spatial resolution (m)	Size	Location
1	KOMPSAT-3A (Subject image)	2015. 10.30	2.2	2000 × 2000	Chang-nyeong-gun (Korea)
	KOMPSAT-3A (Reference image)	2016. 06.18			
2	KOMPSAT-3A (Subject image)	2017. 02.23	2.2	2000 × 1500	Seoul (Korea)
	KOMPSAT-3 (Reference image)	2015. 10.09	2.8		

and 2 times, respectively; the same bands were applied for Site 2 for 7, 1, 4, and 1 times, respectively. Based on these intervals, normalization results were obtained by performing local-based iterative histogram matching. Furthermore, the results of our proposed method were compared with those obtained from the global histogram matching method for a visual and quantitative evaluation. The normalization results are shown in Figs. 4 and 5, and the wasserstein distances are shown in Table 2.

(a) (b)

Fig. 4. Comparison with the results of relative radiometric normalization for Site 1: (a) global histogram matching, (b) proposed method

(a) (b)

Fig. 5. Comparison with the results of relative radiometric normalization for Site 2: (a) global histogram matching, (b) proposed method

Visual evaluation results for both the methods show significantly reduced radiometric differences between the normalized and reference images for the two sites. The overall brightness achieved after the normalization is similar to that of the reference image, and the radiometric consistency is improved compared with the subject image. In particular, it can be clearly observed that the result of local-based histogram matching for Site 1 has more resemblance and consistency with the reference than that obtained with global histogram matching. Although similar overall brightness was achieved by both the matching methods in Site 2 images, local-based histogram matching achieved more similarity with the reference image in the green-colored portions of the vegetation areas. Furthermore, the wasserstein distances of the local-based iterative histogram matching in bands 1, 2, and 3 were shorter regardless of the site, whereas the results for band 4 varied with the site. The vegetation in Site 1 mainly comprises grass, and the performance was slightly reduced in band 4, while for Site 2, which mainly comprises forested areas, the performance was improved in band 4. It is our opinion that band 4 is affected by the type of vegetation, and shows better performance when composed of homogeneous features, such as forests, than of heterogenous features, such as grass.

An additional quantitative accuracy analysis was performed on the radiometric normalization results by manually selecting the invariant pixels, including buildings, rooftops, and roads, from the areas. Then, the NRMSE (Normalized RMSE) was calculated for the selected invariant pixels as shown in Eqs. (8) and (9):

Table 2. Wasserstein distance values of relative radiometric normalization results

Site	Method	Band1	Band2	Band3	Band4	Average
Site 1	Global histogram matching	0.0957	0.0856	0.0963	0.0362	0.0785
	Proposed method	0.0554	0.0605	0.0684	0.0371	0.0554
Site 2	Global histogram matching	0.0128	0.0036	0.0141	0.0096	0.0100
	Proposed method	0.0063	0.0019	0.0131	0.0087	0.0075

$$RMSE = \sqrt{\frac{(y_i^N - y_i)^2}{n}} \tag{8}$$

$$NRMSE = \frac{RMSE}{\overline{y_i}} \tag{9}$$

where y_i^N is the invariant pixels in the normalized image of band i; y_i is the invariant pixels in the reference image of band i; $\overline{y_i}$ is the mean of the invariant pixels in the reference image of band i; and n is the total number of invariant pixels, where 744 and 555 are selected for site1 and site2, respectively. The NRMSE evaluates the accuracy by normalizing the RMSE; thus, lower the NRMSE value, the higher the accuracy of the radiometric normalization. The NRMSE of the subject images and normalized images are shown in Table 3.

The quantitative evaluation also demonstrates that the radiometric variation between the results of both methods decreases when compared with the subject images. When the NRMSE of the subject images is compared with that of the global histogram matching and local-based iterative histogram matching, there is an improvement of 248.25% and 248.81% for Site 1 and 122.81% and 127.09% for Site 2, respectively. Compared with the improvement in the wasserstein distance, this improvement in NRMSE is not significant, because histogram matching is performed based on the distribution of images. In other words, as the normalized pixel values are determined by the transformation of distributions rather than that of pixel values themselves, the pixel value difference between global histogram matching and local histogram matching is not significant. However, this result confirms the usefulness of the proposed method from the point of view of both the visual and quantitative aspects, including for distributions where nonlinear properties are considered.

4. Conclusion

This study proposes a novel method with which to perform normalization on images that contain vegetation differences as an example of nonlinear properties. The proposed method attempts to overcome the main issue of histogram matching that considers only global information. To consider local information, histogram division is first performed according to density, mean, and standard deviation. Further histogram matching is then performed locally using the histogram of the reference image and the wasserstein distance is obtained. The locally matched histogram replaces the subject image and the previous steps are repeated; the latter is further subdivided to account for more local information. The algorithm is repeated until the wasserstein distance no longer improves. Compared with global histogram matching, the radiometric properties of the local-based iterative histogram matching are visually more similar and consistent. Furthermore, the wasserstein distance is significantly improved, and although the NRMSE is not as remarkably improved as the wasserstein distance, it is still considerably improved. In other words, considering the histogram distribution and radiometric properties together, the proposed method produces a better match with the reference images than that obtained by histogram matching that uses global information only. This indicates that the proposed method is applicable when vegetation differences exist in multi-temporal images.

In the future works, the additional usefulness of this method should be identified by acquiring and applying subject and reference images for each sensor, season, and period. In addition, further research on the optimal stopping criterion should be performed by applying distances other

Table 3. NRMSE values of relative radiometric normalization results

Site	Method	Band1	Band2	Band3	Band4	Average
Site1	Raw	0.6440	0.8730	0.8804	1.1102	0.8769
	Global histogram matching	0.2512	0.1799	0.3355	0.2404	0.2518
	Proposed method	0.2518	0.1791	0.3352	0.2397	0.2514
Site2	Raw	0.2706	0.3675	0.2643	0.4219	0.3311
	Global histogram matching	0.1162	0.0945	0.1106	0.2730	0.1486
	Proposed method	0.1162	0.0929	0.1110	0.2632	0.1458

than the wasserstein distance. Finally, change detection should be performed on the normalized images to identify how the change detection can be utilized.

Acknowledgment

This research was supported by a grant (19SIUE-B148326-02) from Satellite Information Utilization Center Establishment Program by Ministry of Land, Infrastructure and Transport of Korean government. Also, this work is financially supported by Korea Ministry of Land, Infrastructure and Transport(MOLIT) as「Smart-City Master and Doctor Course Grant Program」.

References

Bai, Y., Tang, P., and Hu, C. (2018), KCCA transformation-based radiometric normalization of multi-temporal satellite images, *Remote Sensing*, Vol. 10, No. 3, pp. 1-21.

Biday, S.G. and Bhosle, U. (2010), Radiometric correction of multitemporal satellite imagery, *Journal of Computer Science*, Vol. 6, No. 9, pp. 1027-1036.

Chavez Jr, P.S. (1988), An improved dark-object subtraction technique for atmospheric scattering correction of multispectral data, *Remote Sensing of Environment*, Vol. 24, No. 3, pp. 459-479.

Chen, Y., Sun, K., Li, D., Bai, T., and Li, W. (2018), Improved relative radiometric normalization method of remote sensing images for change detection, *Journal of Applied Remote Sensing*, Vol. 12, No. 4, pp. 1-16.

Chen, X. Vierling, L., and Deering, D. (2005), A simple and effective radiometric correction method to improve landscape change detection across sensors and across time, *Remote Sensing of Environment*, Vol. 98, No. 1, pp. 63-79.

Choi, J.W. (2015), Unsupervised change detection for very high-spatial resolution satellite imagery by using object-based IR-MAD algorithm, *Journal of the Korean Society of Surveying, Geodesy, Photogrammetry and Cartography*, Vol. 33, No. 4, pp. 297-304. (in Korean with English abstract)

Du, Y., Teillet, P.M., and Cihlar, J. (2002), Radiometric normalization of multitemporal high-resolution satellite image with quality control for land cover change detection. *Remote Sensing of Environment*, Vol. 82, No. 1, pp. 123-134.

Elvidge, C.D., Yuan, D., Weerackoon, R.D., and Lunetta, R.S. (1995), Relative radiometric normalization of Landsat multispectral scanner (MSS) data using an automatic scattergram controlled regression, *Photogrammetric Engineering and Remote Sensing*, Vol. 61, No. 10, pp. 1255-1260.

Helmer, E.H. and Ruefenacht, B. (2007), A comparison of radiometric normalization methods when filling cloud gaps in Landsat imagery, *Canadian Journal of Remote Sensing*, Vol. 33, No. 4, pp. 325-340.

Hong, G. and Zhang, Y. (2008), A comparative study on radiometric normalization using high resolution satellite images, *International Journal of Remote Sensing*, Vol 29, No. 2, pp. 425-438.

Liu, Y., Yano, T., Nishiyama, S., and Kimura, R. (2007), Radiometric correction for linear change-detection technique: Analysis in bi-temporal space, *International Journal of Remote Sensing*, Vol. 29, No. 22, pp. 5143-5157.

Rabin, J., Peyre, G., Delmon, J., and Bernot, M. (2011), Wasserstein barycenter and its application to texture mixing, *International Conference on Scale Space and Variational Methods in Computer Vision*, 29 May-02 June, Ein-Gedi, Israel, pp.435-446.

Rostami, M., Kolouri, S., Eaton, E., and Kim. K. (2019), SAR image classification using few-shot cross-domain transfer learning, *The IEEE Conference on Computer Vision and Pattern Recognition*, 16-20, June, Long Beach, California, pp. 1-9.

Rubner, Y., Tomasi, C., and Guibas, L.J. (2000), The earth mover's distance as a metric for image retrieval, *International Journal of Computer Vision*, Vol. 40, No. 2, pp. 99-120.

Schott, J.R., Salvaggio, C., and Volhock, W.J. (1988), Radiometric scene normalization using pseudo-invariant features, *Remote Sensing of Environment*, Vol. 26, No. 1, pp. 1-14.

Seo, D.K. and Eo, Y.D. (2018), Relative radiometric normalization for high-resolution satellite imagery based on multilayer perceptron, *Journal of the Korean Society of*

Surveying, Geodesy, Photogrammetry and Cartography, Vol. 36, No. 6, pp. 515-523. (in Korean with English abstract)

Seo, D.K., Kim, Y.H., Eo, Y.D., Park, W.Y., and Park, H.C. (2017), Generation of radiometric, phenological normalized image based on random forest regression for change detection, *Remote Sensing*, Vol. 9, No. 1163, pp. 1-21.

Shakeri, M., Dezfoulian, M.H., and Khotanlou, H. (2018), Density-based histogram partitioning and local equalization for contrast enhancement of images, *Journal of AI and Data Mining*, Vol. 6, No. 1, pp. 1-12.

Song, C., Woodcock, C.E., Seto, K.C., Lenny, M.P., and Macomber, S.Z. (2001), Classification and change detection using Landsat TM data: When and how to correct atmospheric effects?, *Remote Sensing of Environment*, Vol. 75, No. 2, pp. 230-244.

Sun, C.C., Ruan, S.J., Shie, M.C., and Pai, T.W. (2005), Dynamic contrast enhancement based on histogram specification, *IEEE Transactions on Consumer Electronics*, Vol. 51, No. 4, pp. 1300-1304.

Yang, X. and Lo, C.P. (2000), Relative radiometric normalization performance change detection from multi-date satellite images, *Photogrammetry Engineering and Remote Sensing*, Vol. 66, No. 8, pp. 967-980.

Yuan, D. and Elvidge, C.D. (1996), Comparison of relative radiometric normalization techniques, *ISPRS Journal of Photogrammetry and Remote Sensing*, Vol. 51, No. 3, pp. 117-126.

Zhong, C., Xu, Q., and Li, B. (2016), Relative radiometric normalization for multitemporal remote sensing images by hierarchical regression, *IEEE Geoscience and Remote Sensing Letters*, Vol. 13, No. 2, pp. 217-221.